Energy Transfer between Ru(II) and Os(II) Polypyridyl Complexes Linked to Polystyrene†

Cavan N. Fleming, Laurence M. Dupray, John M. Papanikolas,* and Thomas J. Meyer*,‡

Department of Chemistry, The University of North Carolina, Chapel Hill, North Carolina 27599-3290

Received: August 2, 2001; In Final Form: December 3, 2001

Energy transfer between Ru^{II} and Os^{II} polypyridyl complexes covalently attached to polystyrene has been in studied in CH_3CN. The polymer is a 1:1 styrene-*p*-aminomethylstyrene copolymer derivatized by amide coupling with the acid-functionalized metal complexes $[M^{II}(bpy)_2(bpy\text{-}COOH)](PF_6)_2$ ($M^{II} = Ru^{II}$, Os^{II}; bpy is 2,2′-bipyridine and bpy-COOH is 4′-methyl-2,2′-bipyridine-4-carboxylic acid). In the resulting polymer $[co\text{-}PS-CH_2NHCO-(Ru^{II}_{11}Os^{II}_5)](PF_6)_{32}$, 11 of, on the average, 16 polymer sites are derivatized by Ru^{II} and five by Os^{II}. Photophysical properties compared to the homopolymers $[co\text{-}PS-CH_2NHCO-(Ru^{II}_{16})](PF_6)_{32}$ and $[co\text{-}PS-CH_2NHCO-(Os^{II}_{16})](PF_6)_{32}$ reveal that excitation at Ru^{II} is followed by efficient energy transfer to the lower energy Os^{II} sites with near unit efficiency (95%). Time-correlated single photon counting measurements with picosecond time resolution reveal that quenching of Ru^{II*} produced adjacent to an Os^{II} trap site is quenched with an average rate constant $\langle k_{en} \rangle = 4.2 \times 10^8\ s^{-1}$. Ru^{II*} decay and Os^{II*} sensitization kinetics are complex because the polymer sample consists of a distribution of individual strands varying in chain length, loading pattern, and number of styryl spacers. The kinetics are further complicated by a contribution from random walk energy migration. An average energy transfer matrix element of $\langle V_{en} \rangle \sim 2\ cm^{-1}$ for $Ru^{II*} \rightarrow Os^{II}$ energy transfer has been estimated by using emission spectral fitting parameters to calculate the energy transfer barrier.

Introduction

In the development of molecular assemblies for studies in energy conversion, an important issue is the coupling of light absorption to electron transfer indirectly by use of intervening energy transfer in an antenna array.[1−7] One approach to designing such arrays has been to create polymeric and oligomeric assemblies. In our work we have focused on oligopeptides and derivatized polystyrene.[8−13] For the latter, it has proven possible to control intrastrand dynamics by controlling polymer composition and the extent of loading.

In a preliminary account we reported on the existence of facile intrastrand energy transfer in a derivatized polystyrene sample containing a majority of Ru^{II} sites and a minority of Os^{II} sites added as energy traps.[8] The structure of the repeat unit for the metal complex, amide-derivatized polystyrene is illustrated below, **1**. Visible light absorption and photophysical properties in these polypyridyl complexes are dominated by metal-to-ligand charge transfer (MLCT) excited states at 2.1 eV for Ru^{II*} and 1.7 eV for Os^{II*}. These "excited states" are actually a series of low-lying Boltzman populated states that are largely triplet in character.[14,15]

In mixed polymers containing both Ru^{II} and Os^{II}, time-resolved emission and absorption measurements have revealed that excitation at Ru^{II} is followed by rapid, efficient energy migration and transfer to give Os^{II*}. In these experiments Os^{II*} was formed within the instrument response of the apparatus used (fwhm = 10 ns). This was in contrast to an earlier study in which the Ru^{II} and Os^{II} complexes were attached to the polymer backbone by an ether link (**2**) rather than the amide link (**1**) of this study.[11] For **2** it was found that $Ru^{II*} \rightarrow Os^{II}$ energy transfer occurred only between Ru^{II*} and adjacent Os^{II} trap sites. $Ru^{II*} \rightarrow Ru^{II}$ energy migration or self-exchange was slow compared to the natural lifetime of Ru^{II*} with $k_{mig} < 1 \times 10^6\ s^{-1}$.

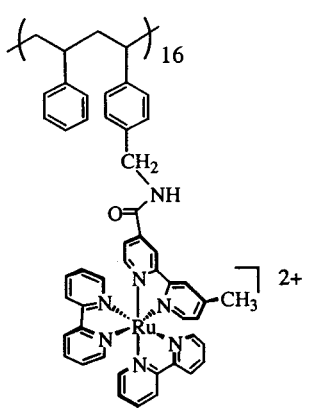

1

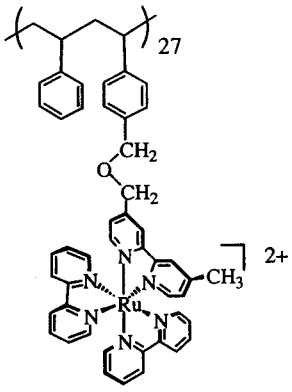

2

In this paper we describe the preparation and characterization of the amide-linked polymer and its photophysical properties including time-resolved measurements at earlier times which demonstrate clearly that quenching of Ru^{II*} is accompanied by the appearance of Os^{II*}. We also provide evidence that the loading ratio of Ru^{II} to Os^{II} was misreported in the preliminary communication, with the actual ratio being on the average of 11 Ru^{II} to 5 Os^{II} sites which somewhat modifies the kinetic interpretation.

Experimental Section

Materials. Spectroscopic grade acetonitrile (Burdick and Jackson) was either used as received or distilled over CaH_2.

† Part of the special issue "Noboru Mataga Festschrift".

* Corresponding authors.

‡ Present address: Los Alamos National Laboratory, MS A127, Los Alamos, NM 87545.

10.1021/jp012990w CCC: $22.00
Published on Web 02/16/2002

Dimethyl formamide (DMF) was distilled from CaH_2 under reduced pressure and stored under nitrogen. Styrene (Aldrich) and *p*-(chloromethyl)styrene (Kodak) were passed through an alumina column prior to use in order to remove the inhibitor. BOP and HOBT were purchased from Novabiochem. All other materials were purchased from Aldrich and used as received.

The following abbreviations are used throughout the paper. b = bpy = 2,2′- bipyridine; b-COOH = 4′-methyl-2,2′-bipyridine-4-carboxylic acid; BOP = (benzotriazoyloxy)tris(dimethylamino) phosphonium hexafluorophosphate; HOBT = 1-hydroxybenzotriazole hydrate; NMM = *N*-methylmorpholine; DMAP = (dimethylamino)pyridine; AIBN = azobisisobutyronitrile. $[Ru(bpy)_2(bpy\text{-}COOH)](PF_6)_2$ and $[Os(bpy)_2(bpy\text{-}COOH)](PF_6)_2$ were prepared as previously described,[16] and were further purified by cation exchange chromatography. Cation exchange chromatography was conducted by using Sephadex CM C-25 as the column support. Sparingly water-soluble salts were dissolved in 9:1 water−acetonitrile mixtures to assist in loading. The eluent consisted of aqueous NH_4Cl solutions buffered to pH 7.0 with sodium phosphates. Pure products were precipitated by addition of NH_4PF_6 to the eluent. Stirring was maintained for 45 min at 0 °C before collection. The solids were washed with cold water followed by anhydrous diethyl ether. The polymer poly(styrene-*p*-(aminomethyl)styrene)(*co*-PS−CH_2NH_2) was prepared as previously described.[17]

[*co*-PS−CH_2NHCO−(Os^{II}_5)]$(PF_6)_{10}$. A solution containing 0.131 g of $[Os(bpy)_2(bpy\text{-}COOH)](PF_6)_2$ (1.3×10^{-4} mol), 0.114 g of BOP (0.260 mmol), 0.025 g of HOBT (0.195 mmol), 20 μL of NMM (0.260 mmol), and 0.015 g of DMAP (1.3×10^{-4} mol) in 4 mL of DMF was prepared and added to 0.1 g of *co*-PS−CH_2NH_2 (2.6×10^{-5} mol) dissolved in 3 mL of CH_2Cl_2. After 2 h at room temperature, the product was isolated by precipitation into an excess of diethyl ether. The polymer was purified from the monomer by dissolving the crude product in CH_3CN and precipitation into aqueous sodium bicarbonate (0.5 M). This last precipitation step was repeated 3 times.

[*co*-PS−CH_2NHCO−$(Os^{II}_5Me_{11})$]$(PF_6)_{10}$. A solution of 1.47×10^{-5} mol [*co*-PS−CH_2NHCO−$(Os_5)](PF_6)_{10}$ and 1.91 mmol of Ac_2O in CH_3CN was maintained at 40 °C for 2 h. Upon addition of the reaction mixture to an excess of diethyl ether, a precipitate formed. The latter was collected by suction filtration, rinsed with diethyl ether, and dried under vacuum. ^{1}H NMR (CD_3CN): δ 0.21−2.7 (m, CH_2−CH backbone, CH_3, 154 H), 4. 22 (s, br., CH_2, 22 H), 4. 45 (s, br., CH_2, 10 H), and 6.21−8.8 ppm (m, styrenic and bipyridyl protons, 270 H); IR (KBr) ν(C═O) = 1668 cm^{-1}.

[*co*-PS−CH_2NHCO−$(Os^{II}_5Ru^{II}_{11})$]$(PF_6)_{32}$. A mixture of 0.037 g of [*co*-PS−CH_2NHCO−$(Os_5)](PF_6)_{10}$ (9.65 μmol), 0.142 g of $[Ru(bpy)_2(bpy\text{-}COOH)](PF_6)_2$ (0.154 mmol), 0.136 g of BOP (0.308 mmol), and 0.031 g of HOBT (0.231 mmol) was dissolved in 3 mL of freshly dissolved DMF. A quantity of 11 μL of NMM (0.308 mmol) and DMAP (0.154 mmol) were added, and the reaction was held for 2 h at room temperature. Isolation and purification were accomplished as described as above. ^{1}H NMR (CD_3CN): δ 0.21−2.64 (m, 154 H), 4. 46 (s, br., 32 H), and 6.17−8.92 ppm (m, styrenic and bipyridyl protons, 512 H); IR (KBr) ν(C═O) = 1668 cm^{-1}; UV−vis (CH_3CN) $\lambda(\epsilon)$ 248 (24 600), 290 (63 800), 458 (15 200), and 614 nm (1280 M^{-1} cm^{-1}).

Measurements. General Methods. UV−visible spectra were recorded on a Hewlett-Packard 8452A photodiode spectrometer. Infrared spectra were recorded on a Nicolet 20DX Fourier transform IR spectrophotometer. ^{1}H NMR spectra were recorded on a Bruker AC200 spectrometer. A Waters 150-CV gel permeation chromatograph with Ultrastyragel columns of 100, 500, 10^3, 10^4, and 10^5 Å porosities in tetrahydrofuran was used for the determination of molar mass and molar mass distribution in the starting polymer samples.

Photophysical Measurements. Acetonitrile (Burdick and Jackson) used in the photophysical measurements was either used as received or distilled over CaH_2. Steady-state emission spectra were recorded on a SPEX Fluorolog-212A photon counting spectrofluorimeter and were corrected for the instrument response. Optically dilute samples ($A_{\lambda(\text{excitation})} < 0.12$) were either freeze−pump−thaw degassed to 10^{-6} Torr or argon sparged for 40 min prior to use. Emission quantum yields were calculated by relative actinometry by using eq 1:[18]

$$\Phi_{sam} = \Phi_{ref}\left(\frac{I_{sam}}{I_{ref}}\right)\left(\frac{n_{sam}}{n_{ref}}\right)^2\left(\frac{A_{ref}}{A_{sam}}\right) \quad (1)$$

where Φ is the emission quantum yield of either the sample or the reference compound, I is the integrated emission profile, n is the refractive index of the solvent, and A is the absorbance in a 1 cm quartz cuvette. The reference was either $[Ru(bpy)_3](PF_6)_2$ for which $\Phi_{em} = 0.062$[19] or $[Os(bpy)_3](PF_6)_2$ for which $\Phi_{em} = 0.005$[20] in acteonitrile at 298 K.

Time-resolved measurements were conducted by time-correlated single photon counting (TCSPC). The apparatus consisted of a mode-locked Nd:YAG laser (Coherent, Antares 76-s) whose frequency tripled output was used to synchronously pump a single jet dye laser (Coherent, 700 series) with Stilbene 3. The dye laser output at 430 nm was cavity dumped to produce ~10 ps pulses. The repetition rate of the dye laser was selected as either 475 kHz (for measurements at 780 nm) with an average power of ~1 mW, or 190 kHz (for measurements at 640 nm) with an average power of 350 μW. The beam was passed through an iris and illuminated without focusing a 10 mm cuvette. The intensity of the incident light was varied by use of ND filters mounted before the monochromator. For luminescence measurements the emitted light was collected at 90° and focused into a single grating monochromator (CVI, Digikrom 240) and subsequently delivered to a cooled, multichannel plate-photomultiplier tube (MCP-PMT) (Hamamatsu, R3809U-51). The signal from the MCP was amplified prior to sending it into a constant fraction discriminator (CFD) (Tennelec, TC454) whose output served as the start pulse for the time-to-amplitude converter (TAC) (Tennelec, TC864). The stop pulse in the timing scheme was obtained by splitting off 10% of the excitation beam and focusing it into a photodiode. The photodiode pulse was sent into a variable delay box, then to the CFD, and finally to the TAC. The TAC's output was sent to a multichannel analyzer (Tennelec, PCA-multiport) which was interfaced to a PC. The instrument response of the apparatus was 80 ps at the fwhm.

Results

Synthesis. The mixed polymer salt [*co*-PS−CH_2NHCO−$(Ru^{II}_{11}Os^{II}_5)](PF_6)_{32}$ was prepared by a previously developed synthetic protocol that involved the binding of five equivalents of the Os^{II} complex $[Os(bpy)_2(bpy\text{-}COOH)]^{2+}$ in the first step. Part of this sample was reacted with acetic anhydride to form acetamide groups at the unreacted amines. The resulting product was characterized by ^{1}H NMR after isolation and purification. The use of high field ^{1}H NMR allows the degree of loading to be ascertained with relatively high accuracy. The procedure is

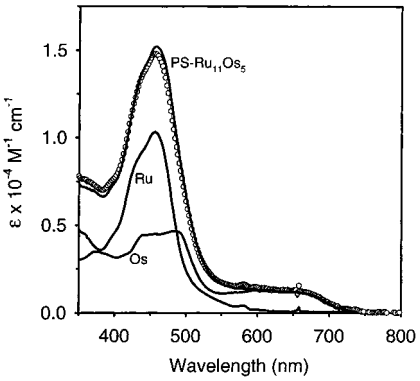

Figure 1. Absorption spectra of [*co*-PS−CH_2NHCO−($Ru^{II}_{11}Os^{II}_5$)]-(PF_6)$_{32}$, and the two model complexes [Ru^{II}(bpy)$_2$(bpy−CONHBz)]-(PF_6)$_2$ and [Os^{II}(bpy)$_2$(bpy−CONHBz)](PF_6)$_2$ scaled by factors of 11/16 and 5/16, respectively, in CH_3CN at room temperature. Also shown is the sum (○) of the two scaled model complex spectra, which matches that of the polymer within experimental error (±5%).

described in detail elsewhere.[17] It involves integration of peak areas for two sets of methylene protons, those linked to the acetamide group and those linked to the complex. The remainder of the sample was allowed to react with a 1.5× excess of the Ru^{II} complex [Ru(bpy)$_2$(bpy-COOH)]$^{2+}$ which resulted in essentially complete binding. Any amine sites that remained unreacted were capped by reaction with acetic anhydride with the total extent of derivatization determined by ^{1}H NMR. Alternatively, the extent of loading can be determined using UV−vis absorption measurements. In a previous account it was reported that the variation of the molar extinction coefficient per repeat unit with loading was not linear.[17] In that work it was claimed that the molar absorptivity of fully loaded [*co*-PS−CH_2NHCO−(Ru^{II}_{16})](PF_6)$_{32}$ was less than the sum of its constituent chromophores. That observation, however, was incorrect. The molar absorptivity does scale linearly with the extent of loading, allowing for the loading ratio to be determined with simple UV−vis absorption measurements.

UV−Visible and CW Emission Spectra. Absorption and emission spectra for [*co*-PS−CH_2NHCO−($Ru^{II}_{11}Os^{II}_5$)](PF_6)$_{32}$ in CH_3CN are shown in Figures 1 and 2 where they are compared with the model complexes [Ru^{II}(bpy)$_2$(bpy-CONHBz)]$^{2+}$ and [Os^{II}(bpy)$_2$(bpy-CONHBz)]$^{2+}$

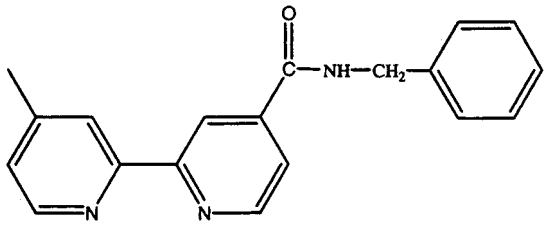

bpy-CONHBz

as PF_6^- salts and the homopolymers [*co*-PS−CH_2NHCO−(Ru^{II}_{16})](PF_6)$_{32}$ and [*co*-PS−CH_2NHCO−(Os^{II}_{16})](PF_6)$_{32}$. In the absorption spectra, ligand-based $\pi \rightarrow \pi^*$ bands appear in the UV and dπ(M^{II}) $\rightarrow$ π^*(bpy) metal-to-ligand charge transfer (MLCT) bands in the visible. The absorption spectrum of the mixed polymer in Figure 1 is the sum of its components. A spectrum constructed from the model complexes at the appropriate ratio matched the spectrum of [*co*-PS−CH_2NHCO−($Ru^{II}_{11}Os^{II}_5$)](PF_6)$_{32}$ to within experimental error (± 5%).

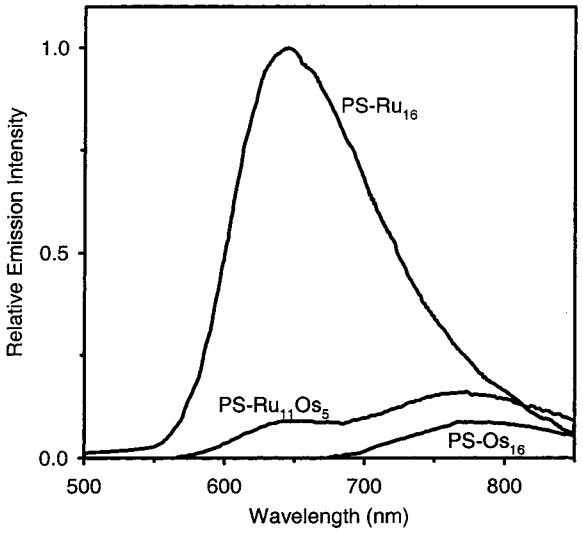

Figure 2. Emission spectra of [*co*-PS−CH_2NHCO−($Ru^{II}_{11}Os^{II}_5$)]-(PF_6)$_{32}$, [*co*-PS−CH_2NHCO−(Ru^{II}_{16})](PF_6)$_{32}$, and [*co*-PS−CH_2NHCO−(Os^{II}_{16})](PF_6)$_{32}$ in argon-sparged acetonitrile at room temperature with 460 nm excitation. Emission profiles have been scaled by their absorbance at 460 nm.

TABLE 1: Parameters Obtained by Application of Eq 3 to Emission Band Shapes for [*co*-PS-CH_2NHCO−(Os^{II}_{16})](PF_6)$_{32}$ and [*co*-PS-CH_2NHCO−(Ru^{II}_{16})](PF_6)$_{32}$ in CH_3CN at Room Temperature[a]

polymer	E_o (cm^{-1})	S	$\Delta\bar{\nu}_{1/2}$ (cm^{-1})	$\hbar\omega$ (cm^{-1})
Os^{II}_{16}	12 860	0.80	1830	1250
Ru^{II}_{16}	15 640	0.89	1880	1350

[a] Uncertainties are ±5% in E_o, S, and $\Delta\bar{\nu}_{1/2}$. The parameter $\hbar\omega$ was fixed at the value indicated and the remaining parameters were varied to obtain the best fits.

Emission spectra shown in Figure 2 were analyzed to calculate the efficiency of $Ru^{II*} \rightarrow Os^{II}$ energy transfer by using eq 2:

$$\eta_{en} = 1 - \frac{\Phi_{Ru_{11}Os_5}}{\Phi_{Ru_{16}}} = 1 - \frac{I_{Ru_{11}Os_5} \cdot A_{Ru_{16}}}{I_{Ru_{16}} \cdot A_{Ru_{11}Os_5}} \qquad (2)$$

which gave η_{en} = 95%. In eq 2, $A_{Ru_{11}Os_5}$ and $A_{Ru_{16}}$ are the absorbances of the mixed polymer and homopolymer at the excitation wavelength, and $I_{Ru_{11}Os_5}$ and $I_{Ru_{16}}$ are the integrated emission profiles of Ru^{II*} in the mixed polymer and homopolymer. The emission spectra of [*co*-PS−CH_2NHCO−(Ru^{II}_{16})](PF_6)$_{32}$ and [*co*-PS−CH_2NHCO−(Os^{II}_{16})](PF_6)$_{32}$ were fit by applying a 1 mode Franck−Condon analysis and eq 3:

$$I(\bar{\nu}) = \sum_{v=0}^{5} \left\{ \left(\frac{E_o - v\hbar\omega}{E_o} \right)^3 \left(\frac{S^v}{v!} \right) \exp\left[-4\ln(2) \left(\frac{\bar{\nu} - E_o + v\hbar\omega}{\Delta\bar{\nu}_{1/2}} \right)^2 \right] \right\} \qquad (3)$$

where $I(\bar{\nu})$ is the emitted light intensity at energy $\bar{\nu}$ in cm^{-1} relative to the emitted intensity at the maximum. As discussed below, the parameters obtained from the fit, E_o, $\hbar\omega$, S, $\Delta\bar{\nu}_{1/2}$ (Table 1), were used to calculate energy transfer barriers. In eq 3, E_o is the energy difference between the $v^* = 0 \rightarrow v = 0$ vibrational levels in the excited and ground state, and $\hbar\omega$ is the quantum spacing for the average medium-frequency acceptor mode fixed at 1350 or 1250 cm^{-1}. S is the electron-vibrational

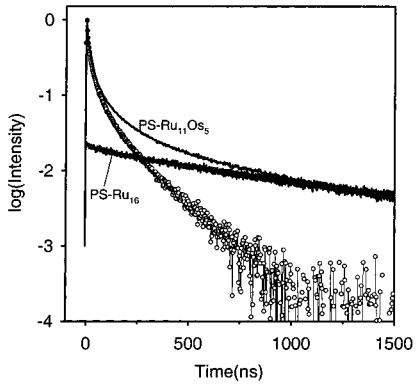

Figure 3. Time-resolved emission from [*co*-PS−CH_2NHCO−($Ru^{II}_{11}Os^{II}_5$)](PF_6)$_{32}$ in argon-sparged acetonitrile at room temperature with 430 nm excitation. The monitoring wavelength was 640 nm. Shown also is the decay for [*co*-PS−CH_2NHCO−(Ru^{II}_{16})](PF_6)$_{32}$ scaled to match the data past 1000 ns for unquenched Ru^{II*} and the result when this curve was subtracted from the mixed polymer data (○).

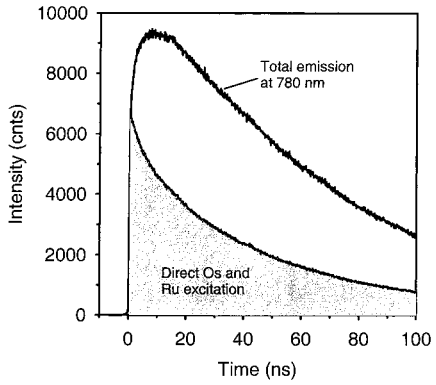

Figure 4. Time-resolved emission from [*co*-PS−CH_2NHCO−($Ru^{II}_{11}Os^{II}_5$)](PF_6)$_{32}$ in argon-sparged acetonitrile at room temperature with 430 nm excitation and monitoring at 780 nm. Also shown as the shaded region is the contribution to the intensity−decay curves due to direct excitation of Os^{II} and Ru^{II}.

coupling constant which is related to the change in equilibrium displacement between states, ΔQ_{eq}, and the reduced mass, M, by $S = (1/2)(M\omega/\hbar)(\Delta Q_{eq})^2$. $\Delta\bar{\nu}_{1/2}$ is the full width at half-maximum of an individual vibronic component.

Emission Decay. Time-correlated single photon counting (TCSPC) was applied to time resolve the decay of Ru^{II*} and growth of Os^{II*} following 430 nm excitation. Figure 3 shows emission decay at 640 nm for Ru^{II*} in [*co*-PS−CH_2NHCO−($Ru^{II}_{11}Os^{II}_5$)](PF_6)$_{32}$. The decay past 1000 ns is monoexponential with a time constant of 900 ns, essentially that of the homopolymer, $\langle\tau\rangle = 980$ ns. The treatment of lifetime data for [*co*-PS−CH_2NHCO−(Ru^{II}_{16})](PF_6)$_{32}$ discussed earlier includes the existence of multiphoton effects.[17] Excited-state decays were dependent on laser power in the range 10−100 μJ/pulse, with lifetimes increasing and becoming more nearly exponential as the energy of the laser pulse was decreased. At the excitation irradiances used in the TCSPC experiment there is no evidence for multiphoton effects over a factor of 3 in incident irradiances.

Shown in Figure 4 is the time-resolved emission decay trace for [*co*-PS−CH_2NHCO−($Ru^{II}_{11}Os^{II}_5$)](PF_6)$_{32}$ following excitation at 430 nm with monitoring at 780 nm. Some of the Os^{II*} growth in Figure 4 occurs within the laser pulse, accounting for ∼65% of the maximum intensity, followed by a slower rise to the maximum at 8 ns. The rapid rise is within the instrument response of the apparatus used (fwhm = 80 ps). Since the absorption bands for Ru^{II} and Os^{II} overlap throughout much of the visible, there is a question as to whether some of this instrument response limited rise is due to fast ($k_{en} > 1 \times 10^{10}$ s^{-1}) energy transfer events or whether it is all due to direct excitation of Os^{II}. The extent of direct excitation of Os^{II} can be determined by comparing the [*co*-PS−CH_2NHCO−($Ru^{II}_{11}Os^{II}_5$)]-(PF_6)$_{32}$ trace at 780 nm with that of [*co*-PS−CH_2NHCO−(Os^{II}_{16})](PF_6)$_{32}$ under the same conditions of concentration and integrated irradiance.

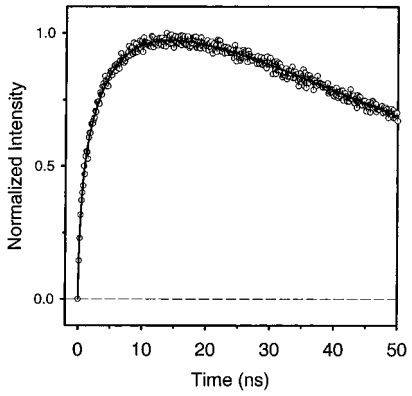

Figure 5. Time-resolved emission from [*co*-PS−CH_2NHCO−($Ru^{II}_{11}Os^{II}_5$)](PF_6)$_{32}$ in argon-sparged acetonitrile at room temperature with 430 nm excitation and monitoring at 780 nm after direct Os^{II} and Ru^{II} excitation are subtracted. The open circles are the experimental data while the line is the result of the fit to eq 4 with the parameters in Table 2.

There is an additional contribution to the fast rise resulting from the overlapped emission bands of Ru^{II*} and Os^{II*} at the monitoring wavelength of 780 nm. This contribution to the transient in Figure 4 can be accounted for since the time scales for excited-state decay of Ru^{II*} and Os^{II*} differ considerably. There is an offset in the baseline past the point where Os^{II*} has decayed completely (∼500 ns) due to Ru^{II*} decay. To account for the Ru^{II*} contribution, the kinetic trace measured at 640 nm, where Ru^{II*} is the sole emitter, is scaled to match the data past 500 ns where only Ru^{II*} photons are detected. The sum of both direct Os^{II} excitation and Ru^{II} emission are shown as the shaded region in Figure 4.

A number of conclusions can be reached on the basis of the data in Figures 3 and 4. (1) Quenching of Ru^{II*} in the mixed polymer is significant with ∼65% decay occurring after 15 ns compared to 10% for the homopolymer. (2) There is evidence for unquenched Ru^{II*} in the 640 nm decay. If this unquenched emission is subtracted, the remaining dynamical events are seen as complete by 1 μs. (3) ∼65% of the Os^{II*} rise occurs on a fast time scale that is within the instrument response and is due to direct excitation of Os^{II} and Ru^{II}.

In treating the dynamics of excited-state formation it was necessary to subtract out the two contributions to the emission transient at 780 nm mentioned above. The result of the subtraction procedure is shown in Figure 5. The kinetics of formation of the Os^{II*} transient are complex and were treated by using a sum of three exponentials and eq 4, In eq 4 *I(t)* is

$$I(t) = \sum_{n=1}^{3} A_n \left(\exp\left(\frac{-t}{\tau_n} \right) \right) \qquad (4)$$

the emission intensity as a function of time t and A is the contribution to the amplitude and τ the time constant for the decay of components 1−3. The best fit parameters are shown

TABLE 2: Kinetic Parameters Obtained by Fitting Emission Decay Profiles to Eq 4[a,b,c]

$Ru_{11}Os_5$	A_1	k_1, s^{-1} (τ_1, ns)	A_2	k_2, s^{-1} (τ_2, ns)	A_3	k_3, s^{-1} (τ_3, ns)
780 nm	0.20	1.5×10^9 (0.670)	0.30	2.9×10^8 (3.5)	0.50	6.7×10^7 (15)
640 nm	0.46	2.2×10^8 (4.6)	0.43	3.6×10^7 (28)	0.10	6.3×10^6 (160)
Ru_{16} (640 nm)	0.20	7.1×10^6 (140)	0.80	9.1×10^5 (1100)		

[a] Data treatment described in the text with monitoring at 780 nm (Os^{II*}) and 640 nm (Ru^{II*}). [b] Excitation is at 430 nm in room temperature CH_3CN. [c] Uncertainties in the kinetic fitting parameters are ±5%.

in Table 2. An average rate constant was calculated for the nonexponential decays by using eq 5,

$$\langle k \rangle = \frac{\sum_n A_n k_n}{\sum_n A_n} \tag{5}$$

For Ru^{II*} decay in the mixed polymer (monitored at 640 nm and shown in Figure 3), the kinetics were also complex. Decay of the residual emission from ~1000 ns and beyond is consistent with decay of the Ru^{II} homopolymer, whose presence in small amount is an expected contribution given the statistical nature of the loading. After subtracting out the homopolymer contribution the remaining decay was fit to eq 4 with the best fit parameters shown in Table 2.

Discussion

The results of the quantum yield and lifetime measurements provide clear evidence for rapid intra-strand $Ru^{II*} \rightarrow Os^{II}$ energy transfer quenching in the mixed polymer [*co*-PS−CH_2NHCO−$(Ru^{II}_{11}Os^{II}_5)$]$(PF_6)_{32}$ in CH_3CN. From the quantum yield measurements, excitation at Ru^{II} leads to Os^{II*} with an efficiency of 95%. This value is independent of excitation wavelength from 420 to 500 nm. At these excitation wavelengths Ru^{II} is the majority light absorber accounting for 69% of the incident light absorbed at 430 nm. Direct excitation of osmium occurs as well but this contribution to the dynamics was independently assessed.

These results demonstrate that the Ru^{II} derivatized polymers can act as efficient "antennas" for collecting visible light and sensitizing a lower energy site on the polymeric backbone. The trapping step occurs by $Ru^{II*} \rightarrow Os^{II}$ energy transfer (k_{en}) and is favored by 0.36 eV. Migration occurs by $Ru^{II*} \rightarrow Ru^{II}$ energy transfer self-exchange (k_{mig}) with $\Delta G^\circ = 0$ and is predicted to be far slower than energy transfer with $k_{en} \gg k_{mig}$.

In a recent study we investigated a related polymer containing a lower concentration of traps per chain in which efficient sensitization of the trap required one or more $Ru^{II*} \rightarrow Ru^{II}$ migration steps for a large fraction of the excitation events.[13]

Energy Transfer Dynamics. Application of TCSPC to wavelengths where Os^{II*} and Ru^{II*} are the dominant or sole emitters provides clear, if semiquantitative insight into intra-strand energy transfer dynamics. Kinetic traces are complex at both monitoring wavelengths, Figures 3−4. To understand the origin of the kinetic complexity it is useful to consider the series of dynamic events that occur following Ru^{II} or Os^{II} excitation.

Given the nature of the polymer synthesis, the formula [*co*-PS−CH_2NHCO−$(Ru^{II}_{11}Os^{II}_5)$]$(PF_6)_{32}$ is an average of a distribution of samples that vary in both chain length and loading patterns. The polydispersity of the underivatized polymer used in the synthesis was 1.53, so that there was a significant distribution of molecular weights. In the sample distribution, there are samples that contain more or less than the average of 5 Os^{II} trap sites. Nonetheless, by considering an average strand of composition, $Ru^{II}_{11}Os^{II}_5$, it is possible to predict that the majority of excitation events will lead either to an excited-state adjacent to a trap or once removed.

[*co*-PS−CH_2NHCO−$(Ru^{II}_{11}Os^{II}_5)$]$(PF_6)_{32}$ was prepared by binding five equivalents of the Os^{II} complex in the first step. Uniform distribution of the Os^{II} sites would minimize steric and/or Coulombic repulsion and result in the possible loading distribution shown in structure **3**. In this structure ~80% of the Ru^{II} excitation events lead to Ru^{II*} adjacent to an Os^{II} trap. The resulting dynamics would reflect primarily $Ru^{II*} \rightarrow Os^{II}$ energy transfer (k_{en}) or a single $Ru^{II*} \rightarrow Ru^{II}$ migration (k_{mig}) step followed by energy transfer. The structure shown in **3** is, of course, only one of many possible loading patterns.

Although qualitative, this analysis is of value in accounting for the transient emission behavior observed for both Os^{II*} and Ru^{II*}. In the intensity−time trace at 780 nm where Os^{II*} is the dominant emitter, a considerable fraction of the initial rise (~65%) is present at our earliest observation time of 80 ps, Figure 4. The prompt rise is due to excitation and production of Ru^{II*} and Os^{II*} during the laser pulse whose contributions to the 780 nm transient are shown as the shaded region. When this component is subtracted from the observed trace, the transient that remains is due only to sensitization events. This transient (Figure 5) reaches a maximum in 15 ns with complex growth kinetics that can be described by a sum of three exponentials (Table 2).

Given the local inhomogeneities in the polymer, a distribution of k_{en} and k_{mig} values is expected. The distribution exists primarily due to variations in the number of spacers between adjacent chromophores and, therefore, the average distance between chromophores for energy transfer or migration. The initial polymer before derivatization was a 1:1 mixture of styryl and 4-chloro-methyl-styryl groups and, on average, there is a single styryl spacer between adjacent chromophores as shown in structure **4**. However, given the random distribution of styryl and derivatized styryl groups, there must be a distribution of local structures including those with no styryl spacers, structure **5**, and those with two, structure **6**, or even more. Given the

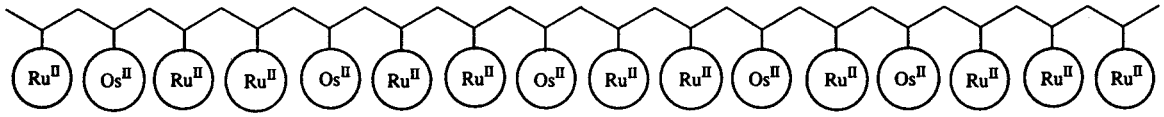

3

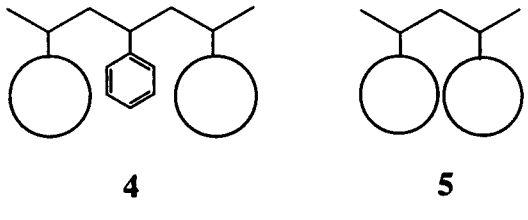

4

5

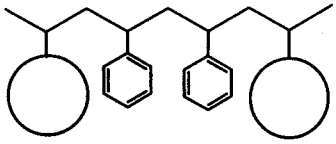

6

distribution in local structures and the expected distance dependence of energy transfer, the triexponential growth kinetics for Os^{II*} represent, at least in part, a distribution of rate constants for the various structures with **4** being statistically dominant. On the basis of the data in Table 2, the average energy transfer rate constant is $\langle k_{en} \rangle = 4.2 \times 10^8\ s^{-1}$.

There is information about $Ru^{II*} \rightarrow Ru^{II}$ migration in the Ru^{II*} decay data in Table 2. There are two distinct regions in the decay traces, a region of quenching dynamics and at longer times a region of unquenched Ru^{II*}, decaying with the characteristic lifetime of $\sim 1\ \mu s$. The unquenched contribution to the intensity−time traces can be subtracted out revealing only the quenching dynamics, as shown in Figure 3. On the basis of this analysis, it is evident that the dynamical events are complete by $1\ \mu s$. It is also revealing that the Os^{II*} decay lifetime is nonexponential and extended to 65 ns compared to the related homopolymer for which $\tau = 49$ ns. This lifetime enhancement can be explained by relatively slow sensitization of Os^{II} by the Ru^{II*} sites once or further removed from the trap with multiple $Ru^{II*} \rightarrow Ru^{II}$ migrations preceding the trapping step.

The same local structural inhomogeneities shown in structures **4**−**6** exist for energy migration and the prediction of a distribution of k_{mig} values. By using the kinetic fit for the Os^{II*} rise and the Ru^{II*} decay data in Table 2, we estimate an approximate time scale for the migration step of 20 ns with $\langle k_{mig} \rangle \sim 5.0 \times 10^7$ which is consistent with the extension in the Os^{II*} decay data.

Energy Transfer Mechanism. On the basis of an earlier molecular modeling study for the related ether-linked polymer, the average periphery-to-periphery, through-space separation distance between nearest neighbors with a single styryl spacer was found to be 7 ± 2 Å and between nonnearest neighbors 20 ± 6 Å.[11] Local segmental motions which decrease the nearest neighbor distance are thermally accessible. Based on these distances, it seems safe to assume that net $Ru^{II*} \rightarrow Os^{II}$ energy transfer is dominated by nearest neighbor events as assumed by the analysis in the previous section. The actual excited-state dipole−dipole distance for energy transfer probably is considerably different for ether and amide-linked polymers **1** and **2**. The chromophoric sites are unsymmetrical with both bpy and substituted bpy as potential acceptor ligands for the MLCT excited state. Transient infrared spectroscopy has been used to show that the amide-derivatized bpy ligand linked to the polymer is the lowest acceptor and the excited-state dipole lies largely along the amide-derivatized pyridyl ring.[21] For ether-linked polymer **2**, bpy is the acceptor ligand and the excited-state dipole lies along one of the Ru−bpy molecular axes away from nearest neighbors on the polymer backbone. It has been suggested that this feature explains the considerable differences in energy transfer and migration dynamics between **1** and **2** with migration more rapid for **1** by a factor of >50.

A wide range of energy transfer rate constants has been reported for related molecular complexes of general form $[(bpy)_2Ru-BL-Os(bpy)_2]^{4+}$ (BL = bridging ligand). The energy transfer dynamics in the Ru−Os dimers are far simpler than in the polymer because the complexes are structurally well defined, there is a single local structure, and quenching occurs in a single step without intervening $Ru^{II*} \rightarrow Ru^{II}$ migration.

Harriman and co-workers have reported $k_{en} = 6 \times 10^{10}\ s^{-1}$ for the para isomer of $[(bpy)_2Ru(bpy-C{\equiv}C-bpy)Os(bpy)_2]^{4+}$.[22] With the more extended 8 Å bridging ligand of 1,4-bis[2-(4′methyl-2,2′-bipyrid-4-yl)-ethyl]benzene, $k_{en} = 1 \times 10^8\ s^{-1}$ in $[(dmb)_2Ru(bpy-etphet-bpy)Os(dmb)_2]^{4+}$.[23] Likewise, in systems involving extended bridges, Balzani et al. estimate $k_{en} = 5.0 \times 10^7\ s^{-1}$ for $[(bpy)_2Ru(bpy-S-py)Os(bpy)_2]^{4+}$ (S is 1,4-bis[2-(2,2′-bipyrid-5-yl)-ethenyl]bicyclo[2.2.2] octane)[24] and $k_{en} = 6.7 \times 10^8\ s^{-1}$ for $[(bpy)_2Ru(bpy-(ph)_3-bpy)Os(bpy)_2]^{4+}$ with a 10 Å bridge.[25]

There are potentially two mechanisms that contribute to energy transfer, Förster (coulomb) and Dexter (exchange). To the extent that the Förster mechanism contributes, the range of values in the molecular systems reflects the differences in separation distance between the initial and final excited-state dipoles. For the Dexter mechanism, the variations with distance comes from the extent of electronic wave function mixing either through space or through the intervening ligand bridge.

For $Ru^{II*} \rightarrow Os^{II}$ energy transfer in the polymers, $\langle k_{en} \rangle = 4.2 \times 10^8\ s^{-1}$. Based on structures **1** and **4**−**6**, even with no spacers, the local through-bond "bridge length" is >20 Å with a region of saturated carbons which disrupts significant electronic wave function mixing through the polymer backbone "bridge".[26] Even with the excited-state dipole lying along the amide-derivatized pyridyl group, there are 15−20 bonds intervening between the excited- and ground-state dipoles.

Based on comparisons with other molecular bridges, the polymer rate constant of $\langle k_{en} \rangle = 4.2 \times 10^8\ s^{-1}$ appears to be unrealistically large for a through-bond pathway. Rather we attribute the energy transfer dynamics to through-space coupling between adjacent chromophores, perhaps mediated by local motions bringing the chromophores into closer contact than the 7 ± 2 Å periphery-to-periphery distance calculated in the earlier molecular modeling study.

Although through-space energy transfer may dominate in the polymer, it is not apparent whether the Förster or Dexter mechanisms dominate or whether both contribute significantly. Given the $1/R^6$ distance dependence predicted for Förster transfer and the exponential dependence for Dexter transfer, Förster transfer is expected to dominate at longer distances and Dexter transfer at shorter distances. However, there is a spin restriction for Förster transfer in that spin must be conserved independently on the donor and acceptor in the energy transfer process. Since the ground states are singlets, to zero order this restricts Förster transfer to singlet−singlet energy transfer. However the MLCT excited "states" are actually a manifold of three closely spaced states, which are triplet or largely triplet in character with varying amounts of singlet character mixed in by spin−orbit coupling.[27] The rate constant for Förster transfer depends on the square of the product of the fraction of singlet spin character in the initial (donor) and final (acceptor) states. This favors Dexter transfer for which either singlet−singlet or triplet−triplet transfer is allowed.[28,29]

On the basis of this analysis, the experimental rate constants for k_{en} and k_{mig} are actually the sums of rate constants from the

manifold of largely triplet states that constitute Ru^{II*} to the manifold of states in Os^{II*}. The individual transitions could occur by a combination of Förster and Dexter transfer from the Boltzmann weighted individual states in the donor to the final states in the acceptor dominated by the three low-lying states mentioned above.

The rate constants for $Ru^{II*} \rightarrow Os^{II}$ energy transfer are related to the emission spectral fitting parameters in Table 1 as shown in eqs 6−7.

$$k_{ET} = \frac{2\pi}{\hbar} V^2 F_{calc} \tag{6}$$

In eq 6, V is the energy transfer matrix element and F_{calc} is the Franck−Condon vibrational overlap factor or Franck−Condon weighted density of states. F_{calc} can be evaluated by using the spectral fitting parameters in Table 1 and eq 7.[30,31]

$$F_{calc} = \frac{1}{(4\pi\lambda_{AD}k_BT)^{1/2}} \sum_{n=0}^{\infty}\sum_{m=0}^{\infty} \exp(-S_D)\exp(-S_A)\left(\frac{S_D^{\,n^*}}{n^*!}\right) \left(\frac{S_A^{\,m}}{m!}\right) \exp\left(-\frac{(\Delta G^\circ + \lambda_{AD}' + m\hbar\omega_D + n^*\hbar\omega_A)^2}{4\pi\lambda_{AD}k_BT}\right) \tag{7}$$

This equation assumes the average mode approximation for both donor and acceptor and the low-temperature limit for the average mode. In eq 7, S_D and S_A are the electron-vibrational coupling constants for the donor (D) and acceptor (A), $\hbar\omega_A$ and $\hbar\omega_B$ are the donor and acceptor quantum spacings, and k_B is the Boltzmann constant. n^* and m are the quantum numbers for excited-state vibrational levels in the donor and ground-state levels of the acceptor. $\Delta G°$ is the free energy change for the energy transfer process. It is related to the 0−0 energies of the donor ($E_{0,D}$) and acceptor ($E_{0,A}$) excited states and the solvent reorganizational energy λ by eq 8.

$$\Delta G° = (E_{0,A} + \lambda_A) - (E_{0,D} + \lambda_D) \tag{8}$$

λ_{AD} in eq 7 is the classical contribution to the barrier and includes the total solvent reorganizational energy and low-frequency modes treated classically. It is given by $\lambda_A + \lambda_D$. These quantities are calculated from the bandwidth parameter $\Delta\bar{\nu}_{1/2}$ obtained by emission spectral fitting and eq 9.

$$(\Delta\bar{\nu}_{1/2})^2 = 16 \ln 2 k_B T\lambda \tag{9}$$

On the basis of eq 7 and the parameters in Table 1, F_{calc} for $Ru^{II*} \rightarrow Os^{II}$ energy transfer is 1.2×10^{-4} and 1.5×10^{-6} for $Ru^{II*} \rightarrow Ru^{II}$ energy migration. With F_{calc} evaluated and $\langle k_{en}\rangle = 4.2 \times 10^8\ s^{-1}$ it is possible to evaluate an average energy transfer matrix element of $\langle V_{en}\rangle \sim 2\ cm^{-1}$ from eq 6. The magnitude of $\langle V_{en}\rangle$ is consistent with values reported for related molecular complexes with V_{en} from 0.6 to 25 cm^{-1}.[22−24] From the approximate rate constant for energy migration of $\langle k_{mig}\rangle \sim 5.0 \times 10^7$, the energy transfer matrix element for migration is $\langle V_{mig}\rangle \sim 5\ cm^{-1}$.

Conclusions

Direct evidence has been obtained for $Ru^{II*} \rightarrow Os^{II}$ energy transfer and $Ru^{II*} \rightarrow Ru^{II}$ energy migration following $Ru^{II} \rightarrow$ bpy MLCT excitation in the polymer [*co*-PS−CH_2NHCO−$(Ru^{II}{}_{11}Os^{II}{}_5)$]$(PF_6)_{32}$ in CH_3CN. The dynamics of both processes are complex because of variations in the loading patterns on individual strands and variations in the number of styryl spacers between adjacent metal complex sites. On the basis of comparisons with chemically linked $Ru^{II*} \rightarrow Os^{II}$ molecular complexes, the mechanism for energy transfer appears to be through-space rather than through-bond, perhaps by a combination of Förster (coulomb) and Dexter (exchange) pathways.

Acknowledgment. The authors thank the Office of Basic Energy Sciences, U.S. Department of Energy (Grant No. DE-FG02-96ER14607) and Los Alamos National Laboratory for support of this research.

References and Notes

(1) Hsiao, J.; Krueger, B. P.; Wagner, R. W.; Johnson, T. E.; Delaney, J. K.; Mauzerall, D. C.; Fleming, G. R.; Lindsey, J. S.; Bocian, D. F.; Donohoe, R. J. *J. Am. Chem. Soc.* **1996**, *118*, 11181.

(2) Wagner, R. W.; Lindsey, J. S. *J. Am. Chem. Soc.* **1994**, *116*, 9759.

(3) Ng, D.; Guillet, J. E. *Macromolecules* **1982**, *15*, 724.

(4) Webber, S. E. *Chem. Rev.* **1990**, *90*, 1469−1482.

(5) Watkins, D. M.; Fox, M. A. *J. Am. Chem. Soc.* **1996**, *118*, 4344−4353.

(6) Whitesell, J. K.; Chang, H. K.; Fox, M. A.; Galoppini, E.; Watkins, D. M.; Fox, H.; Hong, B. *Pure Appl. Chem.* **1996**, *68*, 1469−1774.

(7) Bai, F.; Chang, C.; Webber, S. E. *Macromolecules* **1986**, *19*, 2484.

(8) Dupray, L. M.; Devenney, M.; Striplin, D. R.; Meyer, T. J. *J. Am. Chem. Soc.* **1997**, *119*, 10243.

(9) Slate, C. A.; Striplin, D. R.; Moss, J. A.; Chen, P.; Erickson, B. W.; Meyer, T. J. *J. Am. Chem. Soc.* **1998**, *120*, 4885−4886.

(10) McCafferty, D. G.; Friesen, D. A.; Danielson, E.; Wall, C. G.; Saderholm, M. J.; Erickson, B. W.; Meyer, T. J. *Proc. Natl. Acad. Sci.* **1996**, *93*, 8200.

(11) Jones, W. E.; Baxter, S. M.; Strouse, G. F.; Meyer, T. J. *J. Am. Chem. Soc.* **1993**, *115*, 7363.

(12) Sykora, M.; Maxwell, K. A.; DeSimone, J. M.; Meyer, T. J. *Proc. Natl. Acad. Sci. U.S.A.* **2000**, *97* (14), 7687−7691.

(13) Fleming, C. N.; Maxwell, K. A.; Papanikolas, J. M.; Meyer, T. J. *J. Am. Chem. Soc.* **2001**, *123*, 10336−10347.

(14) Hager, C. D.; Crosby, G. A. *J. Am. Chem. Soc.* **1975**, *97*, 7031.

(15) Kober, E. M.; Meyer, T. J. *Inorg. Chem.* **1984**, *23*, 3877.

(16) Peek, B. M.; Ross, G. T.; Edwards, S. E.; Meyer, G. J.; Meyer, T. J.; Erickson, B. W. *Int. J. Pept. Protein Res.* **1991**, *38*, 114.

(17) Dupray, L. M.; Meyer, T. J. *Inorg. Chem.* **1996**, *35*, 6299.

(18) Demas, J. N.; Crosby, G. A. *J. Phys. Chem.* **1971**, *75*, 991.

(19) Caspar, J. V.; Meyer, T. J. *J. Am. Chem. Soc.* **1983**, *105*, 5583.

(20) Caspar, J. V.; Kober, E. M.; Sullivan, B. P.; Meyer, T. J. *J. Am. Chem. Soc.* **1982**, *104*, 630.

(21) Smith, G. D.; Maxwell, K. A.; DeSimone, J. M.; Meyer, T. J.; Palmer, R. A. *Inorg. Chem.* **2000**, *39*, 893.

(22) Harriman, A.; Romero, F. M.; Ziessel, R.; Benniston, A. C. *J. Phys. Chem. A* **1999**, *103*, 5399−5408.

(23) Shaw, J. R.; Sadler, G. S.; Wacholtz, W. F.; Ryu, C. K.; Schmehl, R. H. *New J. Chem.* **1996**, *20*, 749.

(24) De Cola, L.; Balzani, V.; Barigelletti, F.; Flamigni, L.; Belser, P.; Zelewsky, A.; Frank, M.; Vogtle, F. *Inorg. Chem.* **1993**, *32*, 5228−5238.

(25) Schlicke, B.; Belser, P.; De Cola, L.; Sabbioni, E.; Balzani, V. *J. Am. Chem. Soc.* **1999**, *121*, 4207.

(26) De Cola, L.; Belser, P. *Coord. Chem. Rev.* **1998**, *177*, 301.

(27) Kober, E. M.; Meyer, T. J. *Inorg. Chem.* **1984**, *23*, 3877.

(28) Dexter, D. L. *J. Chem. Phys.* **1953**, *21*, 836.

(29) Speiser, S. *Chem. Rev.* **1996**, *96*, 1953.

(30) Murtaza, Z.; Graff, D. K.; Zipp, A. P.; Worl, L. A.; Jones, W. E.; Bates, W. D.; Meyer, T. J. *J. Phys. Chem.* **1994**, *98*, 10504−10513.

(31) Naqvi, K. R.; Steel, C. *Spectrosc. Lett.* **1993**, *26*, 1761.